Surfaces and Interfaces 26 (2021) 101311

Contents lists available at ScienceDirect

Surfaces and Interfaces

journal homepage: www.sciencedirect.com/journal/surfaces-and-interfaces

Charge transfer uplift in dye-sensitized solar cells using fibrous nanocrystals of platinum-based bimetallic counter electrodes

Muhamad Adam Ramli [a], Elvy Rahmi Mawarnis [b], Marjoni Imamora Ali Umar [c], Mohd Yusri Abd Rahman [a], Vivi Fauzia [d], Muhammad Nurdin [e], Akrajas Ali Umar [a,*]

[a] Institute of Microengineering and Nanoelectronics, Universiti Kebangsaan Malaysia, Bangi, Selangor 43600, Malaysia
[b] Department of Chemistry Education, Faculty of Tarbiyah, Institut Agama Islam Negeri (IAIN) Batusangkar, Batusangkar, West Sumatera 27213, Indonesia
[c] Department of Physics Education, Faculty of Tarbiyah, Institut Agama Islam Negeri (IAIN) Batusangkar, Batusangkar, West Sumatera 27213, Indonesia
[d] Department of Physics, Faculty of Mathemathic and Natural Sciences, Universitas Indonesia, Kampus UI Depok, Depok, West Java 16424, Indonesia
[e] Department of Chemistry, Faculty of Mathematic and Natural Sciences, Universitas Halu Oleo, Kendari 93232, Indonesia

ARTICLE INFO

Keywords:
Bimetal
Poriferous
Counter electrode
Charge transfer
Carrier diffusion
DSSCs

ABSTRACT

Charge transfer dynamic on the surface of a counter electrode (CE) of dye-sensitized solar cells (DSSC) during a photoactivation process relates to the physicochemical properties of the CE. In this paper, we investigated how the co-metal element in the Pt-based bimetallic fibrous nanocrystals (FNC) CE influences the charge transfer dynamic of the dye-sensitized solar cell (DSSC) devices. We discovered that the interfacial charge transfer resistance decreases dramatically in bimetallic CEs if compared with the pristine Pt. For example, it decreases more than 5 times in the AuPt FNC and more than 4 times lower in the AgPt and PdPt FNC CEs. This phenomenon then induced an enhanced carrier diffusion in the device that is reflected by the decrease in the carrier diffusion resistance and the improvement of the carrier lifetime in the device using bimetallic CEs. The DSSCs using the champion CEs, that is AuPt, can produce a short circuit current (J_{sc}), open-circuit voltage (V_{oc}), and fill factor (*FF*) as high as 10.63 $mAcm^{-2}$, 1.00 V, and 0.43, respectively, which correspond to a power conversion efficiency (PCE) of 4.60%. This PCE is approximately 3.5 times higher if compared with the DSSC using the pristine Pt CE. The enhancement of the surface physicochemical properties of the CE due to the bimetallization process is assumed as the key factor for the performance enhancement, the facts that are verified by the X-ray photoelectron spectroscopy and the electrochemical properties analysis results. The synthesis and the device characterization are discussed in detail.

1. Introduction

The nature of redox activity on the surface of a CE plays a critical role in the photovoltaic performance of a DSSC device [1]. The CE that provides a facile charge transfer, active redox reaction of iodide/-triiodide, and has a high electron conductivity enables efficient photoelectrical process in the device. Pt nanostructure has been widely used as CE in DSSC devices due to its excellent electrocatalytic and chemical stability properties. However, owing to its *d*-orbital state band center narrowly lay below the Fermi energy level (ca. −2.19 eV) [2,3], it actively and strongly coordinates with a large range of redox species [4]. This causes its surface-active sites to be vulnerable to a surface poisoning problem, the result of redox species residue contamination. The consequence is its performance in the DSSC will gradually degrade. Therefore, the CE that allows a highly dynamic surface redox activity, which is the existence of facile adsorption and desorption of redox species on the surface of CE, is crucially required for a high-performance and stable DSSC device.

There has been a great deal of effort conducted by many researchers to solve such critical issues in the DSSC utilizing the Pt CEs, such as seeking alternative materials as the CEs, which some of them have been summarized in the literature [5]. They include the use of carbon nanotubes and its doped-systems [6–9], transition metal dichalcogenide based-CEs that include Co—Cu_WS_x nanospheres [10], hierarchical core-shell of Ni-$MoSe_x$/$CoSe_x$ [11], core-shell of N-doped C—CoS_2/MoS_2 nano polyhedrons [12], and $NiSe_2$ [13] and CEs from the reduced-graphene oxide-based system [14–16]. Despite comparable performance with the Pt CE in the DSSCs application have so far been

* Corresponding author at: Institute of Microengineering and Nanoelectronics, Universiti Kebangsaan Malaysia, Bangi, Selangor 43600, Malaysia
E-mail address: akrajas@ukm.edu.my (A.A. Umar).

https://doi.org/10.1016/j.surfin.2021.101311
Received 18 April 2021; Received in revised form 31 May 2021; Accepted 25 June 2021
Available online 1 July 2021

reported, these free-Pt systems CEs still inferior over the Pt-based CEs. Therefore, to re-concentrate using Pt as the CEs and to upgrade its performance by reducing the critical drawback in the surface properties of the Pt CE, particularly via the doping process, should be continuously demonstrated.

Similar to the case of photoanode photoelectrical properties enhancement by doping [17–23], the introduction of the co-metal element into the Pt CEs to form a bimetallic nanostructure has been witnessed as a versatile approach to tune the surface chemistry, electronic density, and physicochemical properties of the CEs [24–27]. The bimetalization process in many cases can overcome the weakness of the individual host metal system and at the same time strengthen the existing properties of the host lattice [28] that are achieved via *d*-orbital mixing, *d*-orbital shape modification, and the band center shifting [27,29]. Thus, highly dynamic redox reactions on the surface and suppressing the active site poisoning can be expected from this process. Enhanced performance in application, particularly in catalysis and DSSCs, has been widely reported using the bimetallic nanostructures-based Pt. For example, the catalytic hydrogenation rate of acetone multiplied for several orders over the AgPt [30,31] and the AuPt [32] catalysts compared with the Pt nanostructured catalyst. Unusual catalytic hydrogenation activity of CO [33], methanol [34], ethylene glycol [35], and proton exchange reaction [36,37] has also been reported over the AuPt and the other Pt-based bimetallic nanocatalysts. In DSSCs, an enhanced performance has also been reported utilizing the Pt-based bimetallic CE [25,38–41].

The effect of metal doping or alloying in the Pt nanostructured electrodes on their electrochemical properties in the DSSC application has been widely presented [40,42]. Nevertheless, the nature of such doping or alloying in the Pt nanostructure with a unique structure, i.e. the fibrous morphology, and its effect on their electrochemical behavior has so far yet to be established. Owing to the quantum effect that has a strong influence on the properties of the materials at this nanoscale regime, bimetallization in the fibrous nanostructure may generate unusual properties that are beneficial for enhanced performance in applications. Here we investigated how the co-metal element in the fibrous Pt-based bimetallic nanostructured CE influences the charge transfer dynamic in the DSSCs device. In this work, by using three models of co-metal ions from the *d*-metal element, that is Au, Pt, and Pd, we established the fact that the *d*-orbital mixing process during the bimetallization strongly modifies the physico-chemistry of the bimetallic CEs. Hence, alter its charge transfer dynamic characteristic in DSSCs. We found that the AuPt, which undergoes an extensive *d*-orbital mixing as revealed by the XPS analysis as its large shift in the chemical states of both Au and Pt, demonstrates much higher enhancement in the charge transfer dynamic than the PdPt and AgPt systems, which have a less intense *d*-band mixing process [43,44]. This process has dramatically lowered the interfacial charge transfer resistance and induced an active carrier diffusion in the device. These resulted in the improvement of the DSSCs performance up to more than four times order higher when using these bimetallic CEs if compared with those utilizing the pristine Pt CE. The best performed bimetallic CE was AuPt and followed by AgPt and PdPt, respectively. As the bimetallization process may also reduce the quantity of the Pt used in the CEs, which is expensive, the fibrous Pt-based bimetallic CEs should be the basis for the fabrication of a low-cost and high-performance DSSCs. The unique interfacial charge transfer dynamic uplift in the bimetallic CEs may find potential application in the growing field of dye-sensitized solar cells.

2. Experimental

2.1. Preparation of the Pt and Pt-based bimetallic fibrous nanocrystals

Platinum-based bimetallic nanocrystal was prepared using our original method for Pt fibrous nanocrystals (FNC) growth directly on a substrate surface, that is a modified liquid phase deposition (LPD) [45,46]. Briefly, in the typical process, the Pt FNC on a fluorine-doped tin oxide (FTO) substrate was realized by submerging a pre-cleaned FTO substrate vertically into a 15 mL growth solution containing 15 mM potassium hexachloroplatinate (IV) (99.9%, Sigma-Aldrich, USA), 10 mM sodium dodecyl sulfate (98%, Sigma-Aldrich, USA), 5 mM formic acid (98%, Sigma-Aldrich, USA) [47]. During the growth process, the solution was kept stirred at 400 rpm on a hotplate with a temperature of 40 °C for 6 h. After that, the substrate was taken out and rinsed with a copious amount of pure water, and then dried with a flow of nitrogen gas. The sample was finally annealed in the air in an electrical oven at 100 °C for 10 min. To grow the Pt-based bimetallic nanocrystals (NC), a 0.67 mM precursor solution of the co-metal ions, that is chloroauric acid trihydrate (99.9%, Sigma-Aldrich, USA), silver nitrate (99.9%, Sigma-Aldrich, USA) and potassium hexachloropalladate(IV) (99.9%, Sigma-Aldrich, USA), was added in to the original growth solution for the formation of AuPt NFC, AgPt NC, and PdPt FNC samples, respectively [30–32,48]. The growth condition and the post-growth treatment followed the Pt FNC synthetic process. Depending on the size of the reaction's container, the growth solution can accommodate up to 6 pieces of FTO substrate of size 1.5 cm × 2 cm.

All chemicals were purchased from Sigma Aldrich and used directly without any purification process. The solution of the reagents was prepared using deionized water (~18.2 MΩ) obtaining from Mili-Q water purification system.

2.2. Preparation of the Tio_2 photoanode

To fabricate a DSSC device to evaluate the effect of the CEs in the photovoltaic process, the TiO_2 nanowalls (TNW) photoanode was prepared using our previously reported method, namely via the liquid-phase deposition method [22,49–51]. The growth of the TNW was carried out by immersing a pre-cleaned FTO substrate into a solution that contains 5 mL of 0.5 M ammonium hexafluorotitanate, $(NH_4)_2TiF_6$, (99.99%, Sigma-Aldrich, USA) and 2 mL of 0.5 M hexamethylenetetramine (HMT) (99.99%, Sigma-Aldrich, USA). The growth process was then performed in a water bath at a temperature of 90 °C for 5 h. The sample was then taken out from the reaction, washed with deionized water, and dried in a flow of nitrogen gas. Finally, the sample was annealed in the air in an electrical oven at 450 °C for about 4 h. All chemicals were purchased from Sigma-Aldrich and used as received.

2.3. Nanostructures characterizations

The morphology of all samples was characterized using FESEM Zeiss Supra 55VP FESEM model with a resolution of 1.0 nm operated at 30 kV. The bi-metallization was examined by mean of X-ray diffraction spectroscopy (XRD) using a Bruker D8 system with CuKα irradiation (λ = 1.541 Å) with a scan rate of 20°/min, X-ray photoelectron spectroscopy (XPS) analysis using Ulvac-PHI XPS Quantera II apparatus with Al Kα (1486.6 eV) monochromatic scanning X-ray source and energy dispersive spectroscopy (EDS). For the case of the XPS analysis results, the results were fitted with a pair of Gaussians–Lorentzian (GL) function overlapping (70% and 30% for Gaussian and Lorentzian components, respectively) with a Shirley-type background. The calculation was calibrated against the C1s element by setting the neutral C1*s* binding energy to 284.8 eV.

2.4. Electrocatalytic properties of the CE

The electrocatalytic activities of the CE were analyzed via a cyclic voltammetry (CV) method using a three-electrode system with a Gamry 1000 interface apparatus. The CVs were carried out in an electrolyte containing 50 mM LiI, 10 mM I_2, and 0.5 M $LiClO_4$ in acetonitrile. The scan rate of 50 mVs^{-1} within a potential window of −0.6 to 1.2 V was used during the measurement. The Ag/AgCl saturated in 2.0 M KCl was used as a reference electrode.

2.5. DSSCs fabrication and characterization

A DSSCs device with a structure of FTO/Photoanode/N719/Electrolyte/CE, where the CE are pristine Pt FNC, AuPt FNC, AgPt NC, and PdPt FNC, was fabricated to evaluate the role of the CEs in the photovoltaic activity of the device. Before the device fabrication, the TiO_2 nanowalls (TNWs) photoanode with anatase phase, prepared using our reported method of liquid-phase deposition [52,53], was immersed into an ethanolic solution of 0.05 mM N719 dye (Sigma Aldrich, USA) for 15 h at room temperature [21,54–59]. The DSSC device was then fabricated by clamping together the photoanode and the CEs using a metal clamp. A parafilm with a thickness of 2 mm and a circle hole of an area of 0.23 cm^2 was sandwiched between the photoanode and the counter electrode. An iodide-tri-iodide couple electrolyte that was obtained from the EL-HPE high-performance electrolyte (Dyesol, Australia) was then injected into the hole. In this study, at least 10 samples were prepared for each device.

The photocurrent (*J-V*) response of the DSSC was examined using a Gamry 1000 potentiostat under the illumination of simulated solar light (AM 1.5) with an intensity of 100 $mWcm^{-2}$ (Newport LC-100 150 W). The charge transfer and transport characteristics of the device were evaluated using electrochemical impedance spectroscopy (EIS). All the characterization conducted in this study was performed in ambient with a temperature of approximately 25 °C and humidity of >70%.

3. Results and discussion

The TiO_2 nanowalls (TNW) photoanode on the FTO substrate have been successfully prepared in this study. The morphology and the structure of the TNW are shown in Fig. 1. The TNW has a morphology of rectangular (Fig. 1a,b) with edge-length and thickness can be up to 50 μm and 100 nm (Fig. 2c), respectively. They grow vertically or tilted from the substrate surface with a random orientation. This has caused a collision amongst the TNW, producing twinning and massive clustering of TNW. Also, as reveals in Fig. 1b,c, the surface of the TNW contains a high-density pore structure that might enable efficient dye adsorption.

The morphologies of the CEs grown on the ITO substrate were shown in Fig. 2. The individual Pt CEs, which is the reference sample in this study, exhibit shape resembling a cubic morphology but with a hairy structure (Fig. 2a). TEM analysis of the structure reveals that the nanocubes is a fibrous structure that is resulted from a hierarchical growth of Pt nanofibers, forming fibrous nanocubes (FNC) (Fig. 2b). Their growth was found to cover the entire substrate surface, enabling the use of them as CEs in a DSSC. The addition of the co-metal element into the Pt host lattice has modified the nanostructure morphology due to the alteration of crystal growth preference, surface segregation, and the growth kinetics that favor the anisotropic growth, the result of the chemistry properties discrepancy as well as the lattice mismatch between the two metals in the bimetallic system [60]. For example, with a lattice mismatch as high as 3.85% and 4.10% with Au and Ag, respectively, the fibrous nanocrystals of pristine Pt transform into a fibrous cauliflower (Fig. 2c,d) and spiky-hierarchical nanofern (Fig. 1e,f) when the Au or Ag ions arebeing introduced into the Pt lattice, respectively. Nevertheless, the morphology and the properties of the nanostructures indicated no visible transformation when the Pd ion is incorporated into the Pt lattice (Fig. 2g,h), the result of identical chemistry and low lattice mismatch, which is 0.85%. The transformation of the morphology, as well as the chemistry of the bimetallic system relative to their individual properties, are expected to enhance the physico-chemistry [61–64] of the CEs for a performance uplift in applications. The surface coverage of the nanostructured bimetallic CEs over the FTO substrate surface is estimated from the FESEM image to be the same, i.e. about 90%. However, the pristine Pt CEs were found to have a little bit lower surface coverage, i.e. ca. 85%. Nevertheless, the thickness of the bimetallic film on the FTO substrate cannot be obtained at this moment due to a limitation in the access to the machine as well as in the technique for cross-section analysis. Nonetheless, judging from the top-view image, we can estimate that the sample of pristine Pt, AuPt, and PdPt CEs should have a more or less similar thickness, namely approximately 200 nm. Meanwhile, the AgPt exhibits much higher thickness as a result of the vertical oriented fern-like structure of AgPt bimetallic. The thickness could be up to 500 nm. Nonetheless, such differences in the CEs thickness are thought to have a limited effect on the charge transfer dynamic on the surface of the CEs, the main feature that is discussed in the work, as this process is strongly related to the structure and the surface chemistry of the CEs.

We then used XRD analysis to confirm the phase crystallinity of the CEs (Fig. 3). As the figure presents, the bimetallic CEs's diffraction

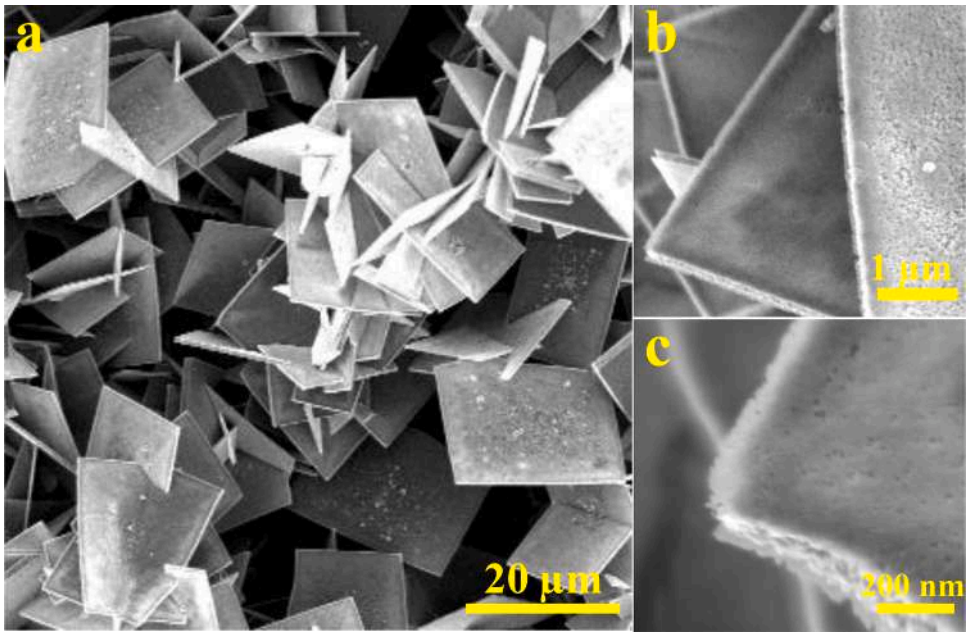

Fig. 1. Morphology of the TiO_2 nanowalls (TNW) photoanode. (a) Low-resolution FESEM image and (b,c) high-resolution images showing the detailed structure of TNW surface.

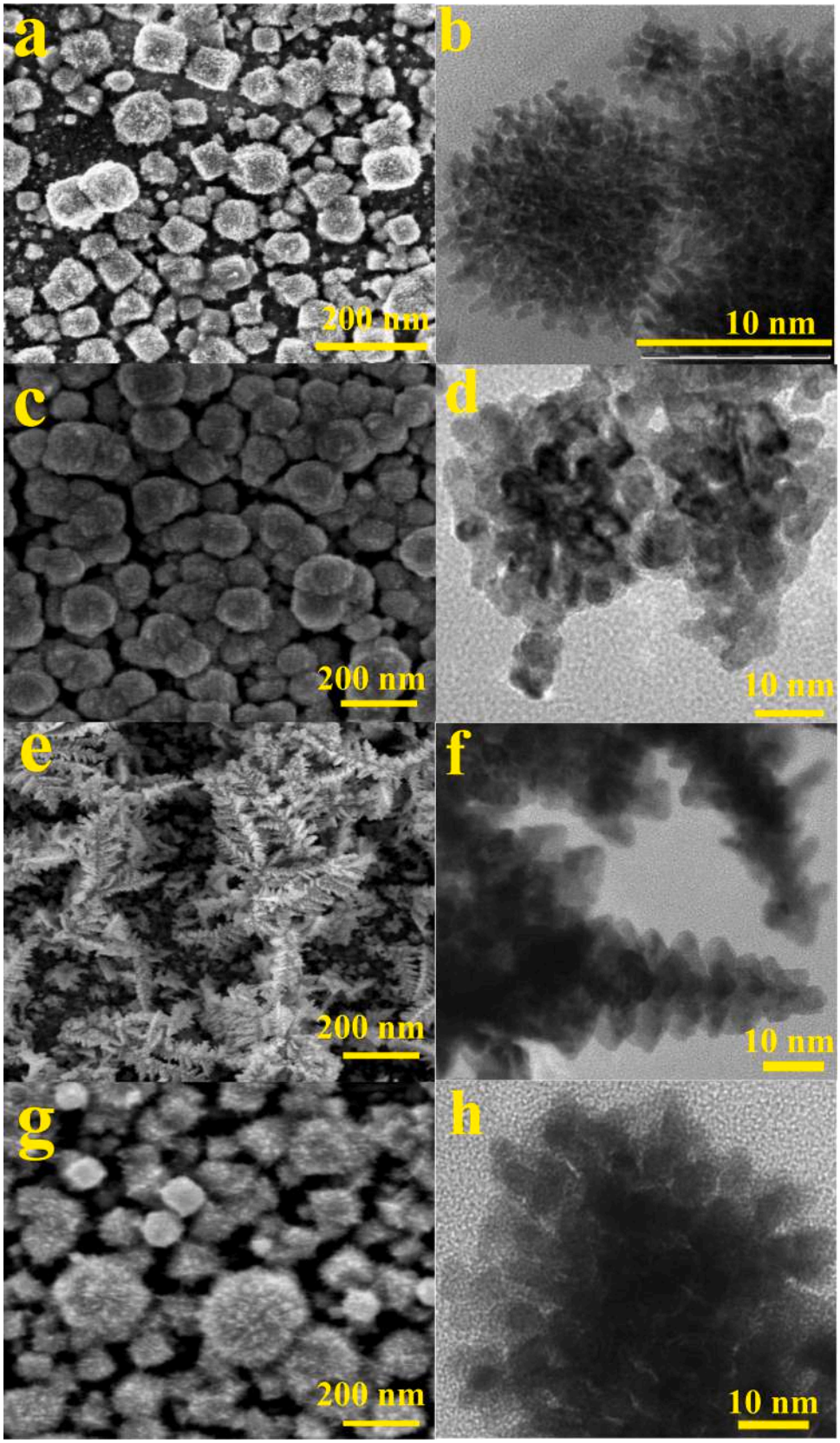

Fig. 2. Typical morphology of the CEs nanostructures. (a-b) pristine Pt NC, (c-d) AuPt FNC, (e-f) AgPt NFn, and (g-h) PdPt FNc. Left and right panel are FESEM and TEM images, respectively.

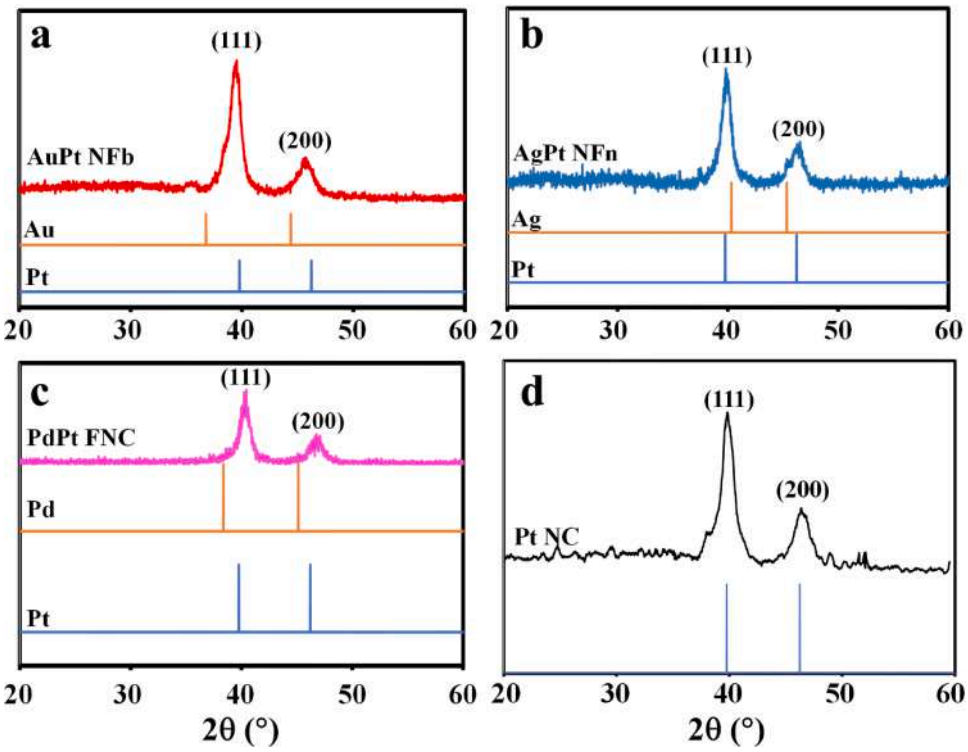

Fig. 3. XRD pattern of the bimetallic nanostructures, namely AuPt NFb (a), AgPt NFn (b), and PdPt FNC (c). (d) XRD pattern for the pristine Pt fibrous nanocubes.

spectra follow a standard diffraction profile for face-centered cubic (fcc) Pt (JCPDS file no: 70-2057) with peaks at 2θ around 40.32 and 46.88° correspond to (111) and (200) Bragg's plane, respectively. Diffraction from the FTO substrate is also observed in the XRD spectra. However, there is a slight displacement in the position of the main peaks of the CEs if compared with the pristine Pt (Fig. 3d). For example, for the case of AuPt, its (111) Bragg's plane diffraction peaks lays in between of (111) peak of Pt and Au, which is 0.25° blue-shift from Pt and 1.33° red-shifted from the Au (Fig. 3a). This fact is one of the evidence that the bimetallization process is occurred, which is due to the existence of distortion of the Pt lattice the result of co-metal element substitution [65]. A similar phenomenon was also witnessed in the case of the AgPt and PdPt (Fig. 3b and c, respectively). The detailed diffraction peaks position of the Pt and the bimetallic system are returned in Table 1. The XPS analysis results (will be discussed later) that show a modification in the binding energy's profile of a particular elemental chemical state is further verification of the existence of bi-metallization in the as-prepared CEs samples [60,66].

Table 1
XRD peaks for the bimetallic nanostructure samples of AuPt NFb, AgPt NFn, and PdPt FNC with a comparison of the individual peaks of the Pt and the co-metal element of Au, Ag, and Pd, respectively.

Samples	(111)	(200)	$I_{(111)}/I_{(200)}$	JCPDS File no.
	2θ			
PtFNC	40.32	46.88	0.72:0.28	
AuPt NFb	39.51	45.66	0.78:0.22	70–2057
Pt	39.76	46.23		70–2057
Au	38.18	44.38		65–2868
AgPt NFn	39.56	46.12	0.73:0.27	–
Pt	39.76	46.23		70–2057
Ag	40.31	45.32		87–7019
PdPt FNC	40.44	46.78	0.72:0.28	–
Pt	39.76	46.23	67.45	70–2057
Pd	38.38	45.15	68.40	35–0681

To further verify the bimetallization process of the samples, we carried out an XPS analysis, and the chemical state of the samples was then compared with the chemical state of the pristine element. The results are shown in Fig. 4. The high-resolution scan at the chemical state of the individual elements in the bimetallic indicates a shifting in the binding energy if compared with the one in the pristine samples. For example, in the case of the AuPt NFBs (Fig. 4a–c), it was discovered that the metallic state of Pt and Au in the bimetal system both shift towards the negative side (lower energy), with respect to their pristine element. That is, the metallic state of Pt in the bimetal (70.79 eV) shifts as high as 0.51 eV if compared with the bulk Pt (71.3 eV). For the case of the Au metallic state of bimetal, it shifts as high as 0.38 eV if compared with the bulk Au binding energy, i.e. 83.62 and 84.00 eV for Au metallic state in the bimetal and the bulk, respectively. A more or less similar tendency was also observed in the AgPt (Fig. 4d-f) and PdPt (Fig. 4g-i) bimetallic systems (See Table 2), which reflects the successfulness of bimetallization process [67,68]. This fact is further verified by the elemental analysis result of the prepared samples (Fig. 5). As the figure shows, the elements in the AuPt, AgPt, and PdPt bimetallic samples are homogeneously distributed over the structures, the condition that only occurs in the bimetallic system. The elemental analysis indicated that the elemental composition in the AuPt is 63.3% and 36.7% for Pt and Au atoms, respectively. While for the AgPt, it is 84.1% and 15.9% for the Pt and Ag, respectively, and for the PdPt, it is 70.2% and 29.8% for the Pt and Pd, respectively.

DSSCs device was then fabricated to evaluate how the co-metals affect the electroactivities of the Pt-based bimetallic nanostructure CEs. Before the device fabrication, the TiO_2 nanowall photoanode was loaded with N719 dye. Fig. 6 shows the typical UV–Vis absorption spectra of the dye-loaded photoanode prepared for the fabrication of DSSCs using different counter electrodes. As can be seen from the figure, the typical absorption band of the dye appears at the region between 450 and 600 nm, confirming an efficient loading of dye onto the photoanode system. As the figure also reveals, the intensity of the absorption characteristic of the dye is more or less similar, indicating the dying method

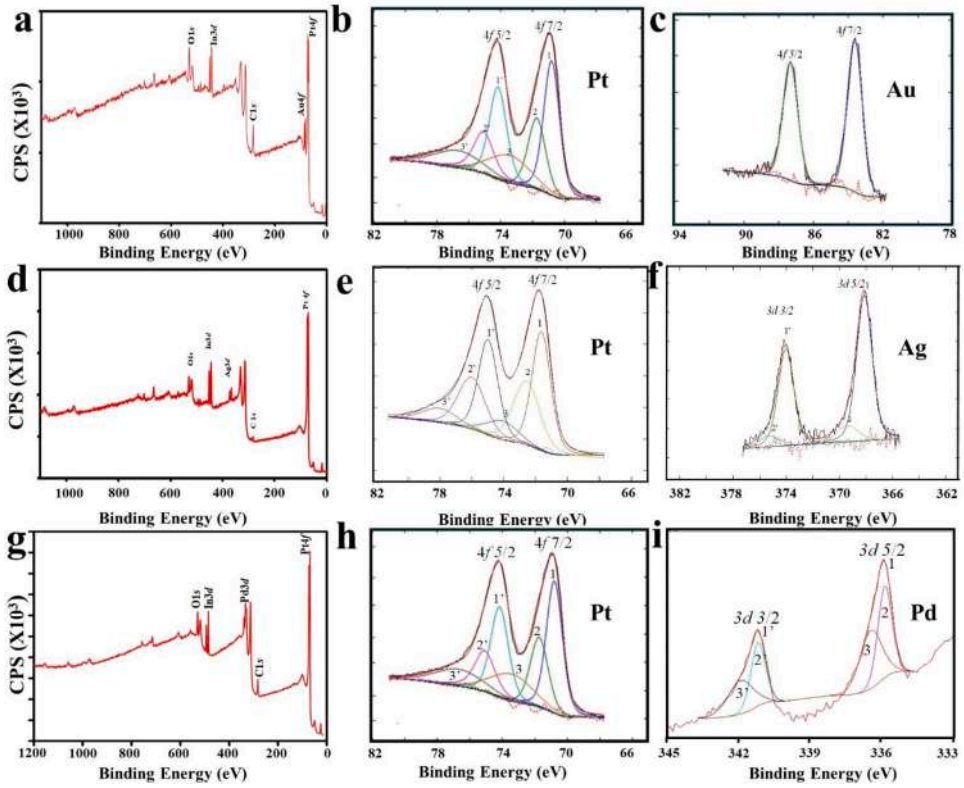

Fig. 4. Low and high-resolution scan spectra of AuPt (a to c), AgPt (d to f), and PdPt (g to i) that are fitted with Gaussian-Lorentzian curves.

Table 2
Metallic state binding energy of bulk metal and bimetallic system. Value in the bracket indicates the shifting in the binding energy relative to their bulk metallic state binding energy.

Bulk metal (eV)				AuPt (eV)		AgPt (eV)		PdPt (eV)	
Pt	Au	Ag	Pd	Pt	Au	Pt	Ag	Pt	Pd
71.30	84.00	368.37	335.00	70.79 (−0.51)	83.62 (−0.38)	71.62 (+0.32)	368.10 (−0.27)	71.62 (+0.32)	335.43 (+0.43)

can produce a homogenous sample for a valid basis of comparing the electroactivities of the CEs.

Fig. 7 shows the typical *J-V* curves of the DSSCs device utilizing the pristine Pt FNC and the bimetallic nanostructure CEs. The photovoltaic parameters of the device are summarized in Table 3. As revealed from Fig. 7 and Table 3, the short circuit current density (J_{sc}) increases upon the introduction of co-metal elements into the pristine Pt host lattice. The highest J_{sc} recorded were in the DSSC using the AgPt NFn CE, which is as high as 11.01 ± 0.02 mAcm^{-2} and followed by the devices using the AuPt and PdPt CEs with J_{sc} as high as 10.63 ± 0.02 and 9.52 ± 0.02 mAcm^{-2}, respectively. Regarding the open-circuit voltage (V_{oc}), the devices utilizing the AgPt and PdPt exhibit a small decrement compared with the ones using the pristine Pt CEs. Nevertheless, the V_{oc} values of these devices more or less lay in the same narrow range region, that is from 0.63 to 0.73 V. It is understood that the decreasing of the V_{oc} value in the AgPt and PdPt based devices should be the result of the tradeoff between the V_{oc} and J_{sc}, where in most case the increasing of J_{sc} will decrease the V_{oc} [69–72]. As their higher J_{sc} values, eventually, the power conversion efficiency of the AgPt- and PdPt-based DSSCs are higher than the pristine Pt-based DSSC. Despite the V_{oc} exhibits declining upon using the AgPt and PdPt CEs, it is significantly enhanced in the AuPt based DSSC devices. The V_{oc} as high as 1.00 V was recorded using the AuPt CEs. Regarding the fill factor, all the devices indicated a more or less similar value that lay at the range of 0.37 to 0.43. Based on these results, it can be remarked that the highest PCE is produced by the AuPt based device with PCE as high as 4.60 ± 0.07%, and followed by the AgPt and PdPt based devices with PCE as high as 2.95 ± 0.07% and 2.22 ± 0.07%, respectively.

The V_{oc} of the device is determined by many factors including, the charge transfer dynamic, density of state or energetic disorder, donor-acceptor interface, and energy level alignment, carrier density, etc. [73]. In general, it mainly describes the nature of photoelectrical dynamic in the device, particularly related to the carrier recombination, which in practice is proportional to the photo-generated current density and inversely proportional to the saturated current density (minority carrier at donor and acceptor) of the device. The V_{oc} can have a maximum value as high as the differences between the HOMO level of the donor and the LUMO level of the acceptor. In the device with higher photo-generated current density due to the enhancement of the charge transfer dynamic at the CEs, such as in the AgPt and PdPt based device, the saturation current density may also raise proportionally or higher than the photogenerated current density, lowering the V_{oc} value. However, in this case, the reduction of the V_{oc} value is relatively small compared to the V_{oc} of the reference device. In the case of the AuPt CE-based device, both J_{sc} and V_{oc} are improved if compared to the reference device. This is attributed to the development of an impressive electrical field built-up in the device due to enhanced interfacial charge transfer activities at the CEs, promoting a highly dynamic photo-generated carrier that can overcome the saturation current density as well as the carrier recombination. This improves both the

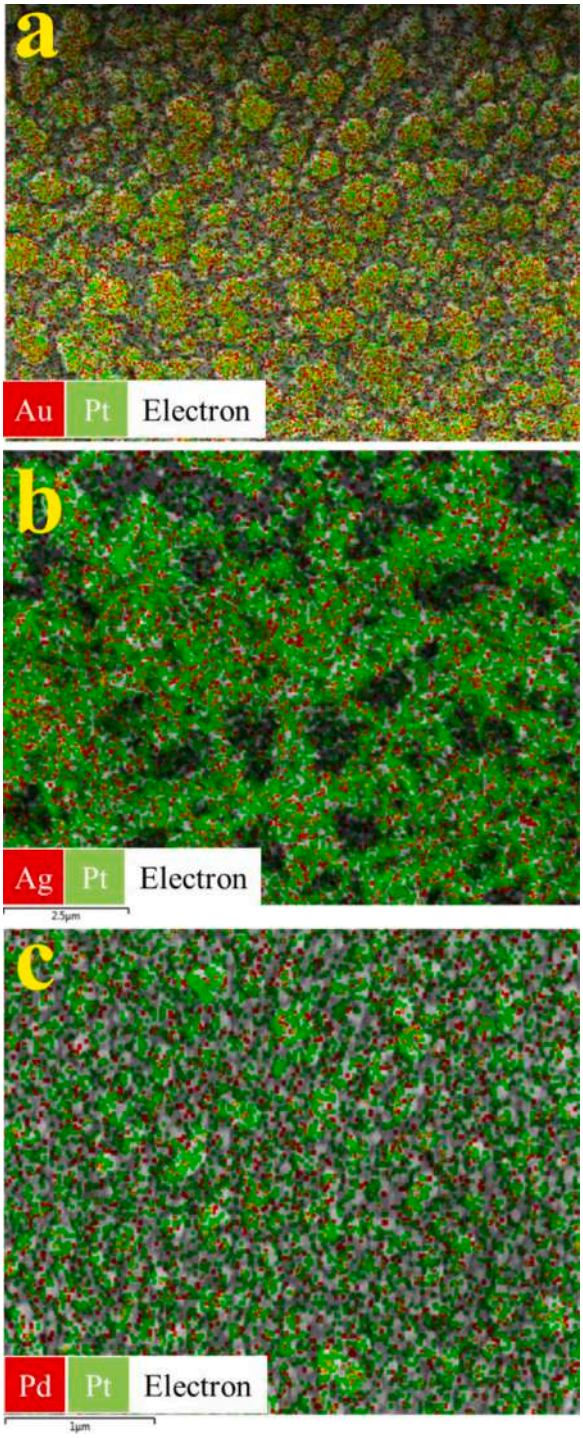

Fig. 5. EDX elemental mapping spectra of bimetallic nanostructure samples namely (a) AuPt NFb (b) AgPt NFn and (c) PdPt FNC.

photo-generated carrier and the V_{oc} of the device.

The superiority of the bimetallic-based CEs over the pristine Pt CE can be explained according to the following facts: Firstly, the enhancement of the charge transfer process in the bimetallic CEs. We have carried out EIS analysis using a non-symmetric three-electrode system to verify this process where it can selectively acquire the nature of surface activity over the working electrode regardless of any kinetic process that occurred at the bulk of the solution [74] or the characteristic of the mass transport or potential change over the CE, in which the latter two can be accurately estimated using symmetric cell configuration as presented in

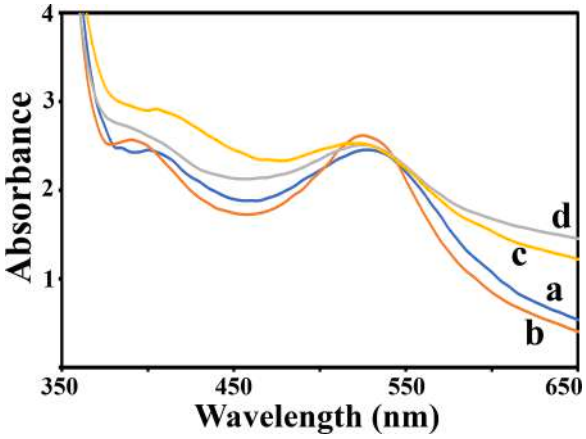

Fig. 6. Absorption spectra of dye (N719)-loaded TiO_2 nanowalls photoanode for DSSCs device fabrication using Pt (a), AuPt (b), AgPt (c), and PdPt (d) counter electrodes.

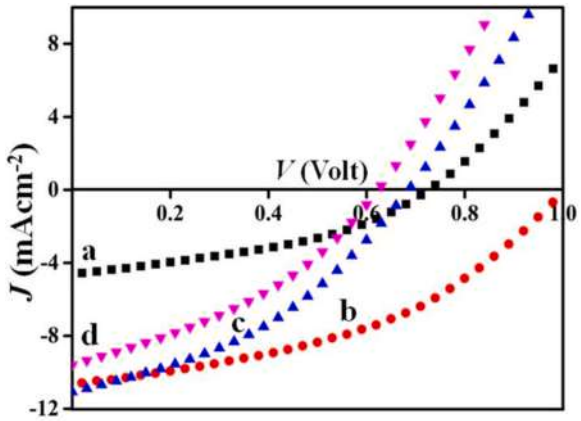

Fig. 7. J–V curves of DSSCs utilizing CEs of pristine Pt NC (a) and different bimetallic nanostructure counter electrodes, namely AuPt NFb (b), AgPt NFn (c), and PdPt FNC (d), under solar light illumination (AM1.5) at 100 mW cm^{-2}.

Table 3
Photovoltaic and electrochemical parameters of DSSCs utilizing pristine Pt NC and bimetallic nanostructure as CEs.

Sample	Pt NC	AuPt NFb	AgPt NFn	PdPt FNC
Photovoltaic parameter				
J_{sc} (mAcm^{-2})	4.62 ± 0.18	10.63 ± 0.02	11.01 ± 0.02	9.52 ± 0.02
V_{oc} (v)	0.73 ± 0.01	1.00 ± 0.01	0.69 ± 0.01	0.63 ± 0.01
Efficiency (%)	1.33 ± 0.08	4.60 ± 0.07	2.95 ± 0.07	2.22 ± 0.07
Fill Factor	0.39 ± 0.02	0.43 ± 0.01	0.39 ± 0.01	0.37 ± 0.01
Lifetime (ms)	35.84	314.86	122.40	125.44
Electrochemical parameter				
E_{red1} (V)	0.21	0.29	0.27	0.25
J_{red1} (mAcm^{-2})	3.91	8.64	13.03	8.54
E_{ox1} (V)	0.70	0.83	0.82	0.76
E_{pp} (V)	0.49	0.54	0.55	0.54
R_s (Ω)	70	70.5	74	71
R_{ct1} (Ω)	2.83	0.52	0.59	0.62
R_{ct2} (Ω)	21.90	13.40	14.10	14.40

an earlier review in this topic [75], so that the role of the co-metal element in the bimetallic electrode surface activities can be deduced. The results are shown in Fig. 8a and Table 3. As judged from Fig. 8a, the

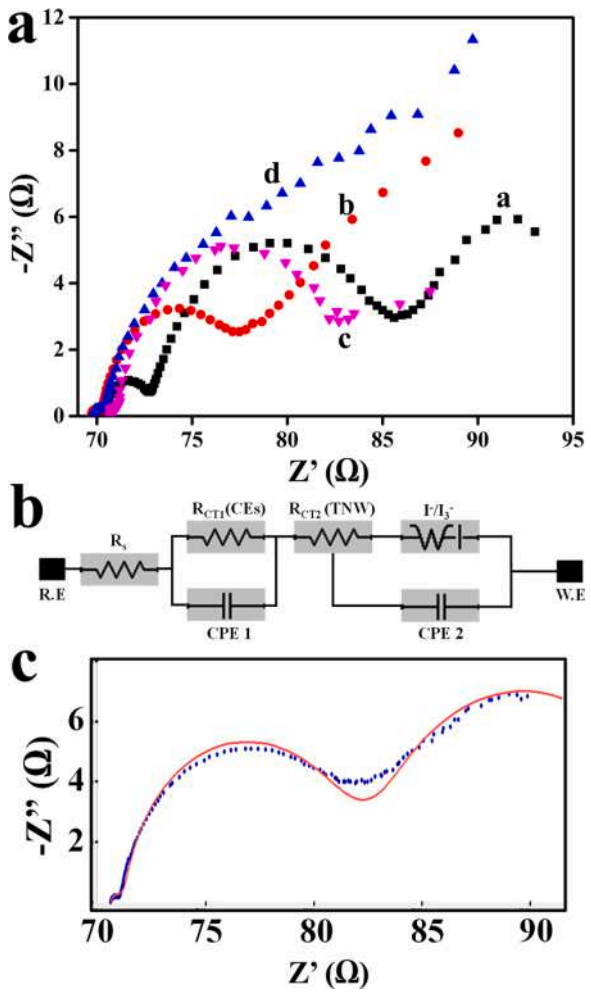

Fig. 8. (a) EIS spectra of the devices (curve a to d are EIS spectra for devices using Pt, AuPt, AgPt and PdPt CEs, respectively). (b,c) The equivalent circuit and the typical curve fitting profile of EIS spectra.

interfacial charge transfer resistance (R_{ct1}), reflected by the semicircle at the high-frequency region, of the DSSCs decreases when the bimetallic CEs employed in the device. By fitting the result using an equivalent circuit as shown in part b of Fig. 8 (with the typical fitted result is shown in Fig. 8c), it is found that the lowest R_{ct1} was obtained from the DSSC utilizing AuPt (curve b) as CEs with values as low as 0.52 Ω and it is followed by the AgPt (curve c) and PdPt (curve d) with R_{ct1} values of 0.59 and 0.62 Ω, respectively. Meanwhile, the R_{ct1} is as high as 2.83 Ω in the pristine (curve a) CEs based device. This is equivalent to the enhancement of charge transfer dynamic up to more than 5 times higher in the bimetallic CEs, particularly in the AuPt CEs. Because the semicircle is also influenced by the constant phase element 1 (CPE1), which is low in value, it is further verified that the CE also enables facile charge collection and transport as it features a relatively low electrochemical capacitance of the device system that renders a limited charge accumulation at the CE interface, the possible result of the CE's quantum capacitance enhancement [20,76]. The enhancement in the charge transfer characteristic of the CE also causes an active charge-transfer dynamic at the TNW–dye/electrolyte interfaces and redox species diffusion in the electrolyte, as indicated by the low value of Nernst diffusion impedance (Z_w) of the electrolyte [48]. This can be seen by the small diameter of the semicircle in the middle frequency region of the spectrum which represents R_{ct2} and CPE2. Also, the semicircle in the low-frequency region shows relatively low in diameter and this region represented the Warburg element in the equivalent circuit. Thus, facile charge transfers between the interfaces in the devices increase the whole performance of the device. From the analysis, it is also recorded that the sheet resistance (i.e. combination of sheet resistance at photoanode and CEs system) is comparable with each other with a value of approximately 70, 70.5, 74 and 71 Ω for the pristine Pt, AuPt, AgPt and PdPt CEs, respectively. As both the substrate of the photoanode and the CEs are FTO with a sheet resistance of approximately 15 Ω/square, it can be estimated that the sheet resistance of the CEs is from 40, 40.5, 44 and 41 Ω for the pristine Pt, AuPt, AgPt and PdPt, respectively. There is indeed discrepancies in the sheet resistance value of the CEs, but it is relatively low, i.e. from 0.5 to 5 Ω respected to the pristine Pt CE. This certainly gives a negligible influence to the interfacial charge dynamic on the surface of the CEs.

These phenomena may be further explained using the cyclic voltammetry (CV) analysis results as presented in Fig. 9. As the figure reveals, the CV curve shows the existence of one oxidation peak at 0.77 V and two reduction peaks at 0.65 V and −0.28 V. The oxidation peak at 0.77 V is associated with the oxidation of I_3^-/I_2. Meanwhile, the two reduction peaks are related to the reduction of I_2/I_3^- and I_3^-/I^-, respectively. In a normal case, the CV of I^-/I_3^- should have two couple of redox pairs. Therefore, the one oxidation peak, i.e. I^-/I_3^- oxidation, which is normally at 0.4 to 0.5 V, is not observed in this work. This could be due to the effect of the active site blockage by the residual chloride ions formation on the surface of the CEs that was produced during the synthetic process using the $PtCl_6^-$ precursor, which limits the I^-/I_3^- oxidation, a phenomenon that is also observed in the recent literature [77]. As the figure also shows, the redox peak to peak separation (E_{pp}) is higher in the bimetallic CEs, due to the modification of the work function of the pristine Pt upon bimetallization [78]. Despite this fact, the enhancement of the Faradaic current density (J_{red}) in the bimetallic CEs verifies the improvement of charge transfer activities in these CEs systems, increasing the overall performance of the DSSCs devices. It is true that in this case the AgPt NFn indeed presents the highest J_{red} (see), but, due to its larger work function mismatch with the redox species, as revealed by its E_{pp} value, the V_{oc} of the device using the AgPt CE decreases, lowering the PCE.

We then performed a Tafel polarization analysis to further confirm the detailed nature of the charge transfer dynamic over the CEs electrode. The results are shown in Fig. 10. As the figure reveals, the diffusion activity of redox species (I^-/I_3^-), which is represented by the J_{lim}, and the electrocatalytic activity (represented by the J_0, i.e. tangential line to the offset potential region on the cathodic polarization zone with the Tafel zone line) dramatically increase if the bimetallic CEs are used, enhancing both the charge transfer and transport in the device

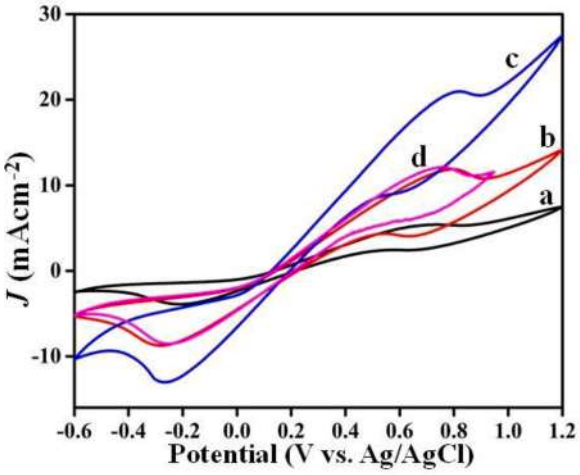

Fig. 9. CV curves of DSSCs utilizing CEs of pristine Pt NC (a) and different bimetallic nanostructure namely AuPt NFb (b), AgPt NFn (c), and PdPt FNC (d) in an electrochemical cell containing I^-/I_3^- electrolyte at room temperature and a scan rate of 50 mV s^{-1}.

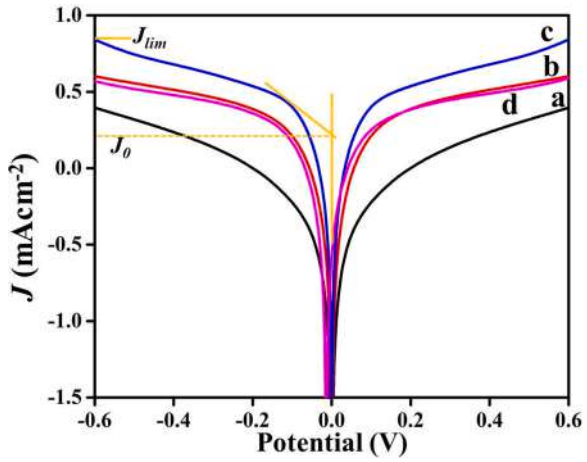

Fig. 10. Tafel polarization curves of DSSCs utilizing CEs of pristine Pt NC (a) and different bimetallic nanostructure namely AuPt NFb (b), AgPt NFn (c), and PdPt FNC (d).

[79,80]. This is parallel with the EIS result presented in Fig. 8 as the fact of J_o and J_{lim} are proportional to the inverse the R_{ct} and the Nernst diffusion resistance, respectively, confirming the enhanced charge-transfer dynamic over the bimetallic CEs.

We are aware that the use of an aqueous reference electrode, i.e. Ag/AgCl (in saturated KCl), in an aprotic nonpolar solvent of acetonitrile might produce a less accurate description of the electrochemical properties of the working electrode system due to the existence of an open circuit potential drift that is related to the liquid-liquid heterojunction issue [81], particularly if used under a long-period of measurement. Despite that fact, the potential drift is relatively low of which only fluctuates around 0.3 V/min [82]. This implies that the electrochemical behavior of an electrode system obtained via this measurement is acceptable as the measurement was carried out within a very short-term period. Besides, owing to the entire measurement were carried out under a similar condition, the electrochemical performance of the electrodes studied in this work can be compared with. With a relatively small open circuit potential drift, the present electrode performance should also be weighed up with the recently reported results.

While the electrochemical analysis results reveal the nature of interfacial charge transfer dynamic uplift in the device using the bimetallic CEs, the XPS analysis results (Fig. 4) indicate the detailed modification of the electronic properties of the Pt in the bimetallization process. The addition of co-metal elements into the Pt lattice system has disrupted the *d-d* orbital symmetry and the band center relative to the Fermi level that is indicated by the shifting in the binding energy from the pristine Pt, modifying the chemistry of the nanostructure surface [83]. In addition, the existence of lattice mismatch between the metallic element induces a change in the crystal growth preferential, producing an exotic and highly anisotropic nanostructure system that contains high-density active sites [84]. This feature causes the catalytic process to become active and rapid which can increase the catalytic reaction over the surface of the bimetallic samples. This process is predicted to be more active as the presence of the fibrous structure of the CEs of which provides a large surface area for the interfacial charge transfer process.

Owing to the existence of the above-mention phenomena, the charge transfer at the device's interfaces becomes highly active and facile of which then promotes a long carrier lifetime, enhanced the quantum capacitance for rapid carrier transport, and limited recombination at the interface, the phenomena that are verified by the Bode plot and the dark current analysis. It also can be seen from Bode plot results that the maximum frequency of the AuPt NFb samples shifts to the lower frequency region, reflecting the high diffusion rate of electrolyte on the surface of the CE, which also reflects an improved interface contact between the electrolyte and the CE for an active interfacial charge transfer process. By using the frequency maximum in the Bode plot (part A of Fig. 11), the carrier lifetime in the AuPt FNC CEs based device was found to be as long as 132.48 ms. Meanwhile, the lifetime for the AgPt and PdPt CE-based devices is as long as 314.86 and 125.44, respectively. These values are more than 7 times to almost 20 times higher than the carrier lifetime in the pristine Pt CE-based devices (15.9 ms). Such a process is likely supported by a low photogenerated carrier recombination properties of the device in the bimetallic CEs system, a phenomenon that is revealed by the high threshold voltage (~1 V) of the dark current (part B of Fig. 11). It is true that the carrier recombination process largely occurs in the semiconducting photoanode system. However, a positive carrier injection (forward charge transfer process) at the electrolyte/CE interface is required to drive effective carrier transportation and separation via the build-up of high electrical potential differences across the device. Thus, the CEs with low charge transfer resistances are necessary to lower the photogenerated carrier recombination in the device.

It has been confirmed that the bimetallization has effectively promoted a highly active charge transfer in the device, improving the power conversion efficiency. This performance's enhancement was also found to depend on the co-metal sample used in the Pt-based bimetallic CEs. For example, we take the case of the AuPt and the AgPt CEs based devices in this study. As mentioned early, the AuPt and the AgPt CEs based device realized improvements in the charge transfer dynamic up to more than 5 and 4 times, respectively, higher than the control device. Meanwhile, their PCE's enhancements are only 3.5 and 2.2 times from

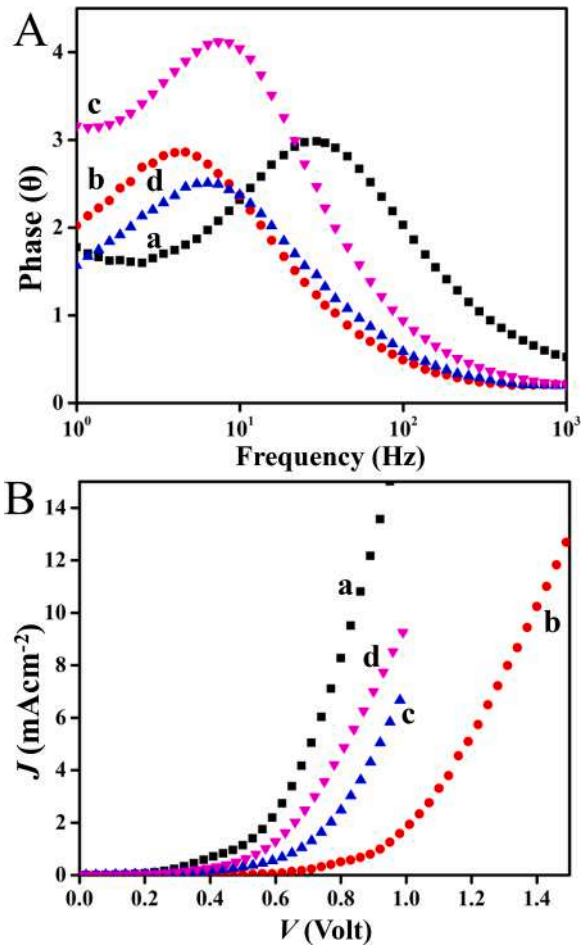

Fig. 11. Bode plot (A) and J–V curves in dark conditions (B) from DSSC devices utilizing CEs of pristine Pt NC (a) and different bimetallic nanostructure namely AuPt NFb (b), AgPt NFn (c) and PdPt FNC (d).

the control device for AuPt and AgPt CEs based devices, respectively. Nonetheless, as normal in the solar cells device, the enhancement in the interfacial charge transfer dynamic is not always linearly followed by the PCE of the device due to the PCE depends on the combinative effect of the nature of the charge transfer as well as the charge separation and recombination kinetics in the device. While the enhancement of the interfacial charge transfer dynamic magnifies the photocurrent density (J_{sc}), the nature of recombination kinetic at the interface affects the V_{oc}, where an active recombination kinetic decreases the V_{oc} and vice versa, a limited recombination activity increases the V_{oc}. On this basis, it can be noted here that: (i) The recombination kinetic in the AuPt CEs based device is low and at the same time, its interfacial charge transfer dynamic is enhanced as its V_{oc} as well as J_{sc} considerably intensify if compared with the control device. (ii) In the meantime, the other bimetallic CEs based devices might suffer from active interfacial recombination as their V_{oc} is lowered in respect to the control device despite the existence of enhanced charge transfer dynamic in these DSSC devices. Nevertheless, we are aware that the fill factor of all the devices is relatively low and inferior to the recently reported high-performance DSSCs [85,86]. There have been several factors that influence the fill factor, particularly the quality of the photoanode and the CEs layers and the electrolyte thickness or the distance between the photoanode and the CEs. However, in our present case we thought that the low fill factor could be due to related to the thickness of the electrolyte in which, due to a technical restriction of the device fabrication, we used the electrolyte thickness as thick as 2 mm. This is much thicker compared with the optimal case (in the order of tens of micrometers) and is too thick to maintain a proper ion dynamic as well as mass transport in the electrolyte. Thus, carrier loss due to ion dynamic and mass transport issues is high, reducing the fill factor. Despite these facts, the role of co-metal in the electrocatalytic activities of the bimetallic CEs can be deduced.

Nevertheless, there have been multiple factors besides the effect of the improvement of the electrocatalytic activities of the CEs for the improvement of the performance, such as the light-scattering effect by the CEs. However, under the present case of which the thickness of the electrolytes far exceeds the optical field of the scattered light, the improvement of Jsc by expanded excitation of active materials by the scattered light is assumed to be limited and to have a minute impact. Thus, the improvement of interfacial charge transfer dynamic the result of special properties of CEs should be the key factor for the performance improvement.

We also have evaluated the performance of the best device, i.e. AuPt CEs based-device, during 32 weeks aged under an ambient condition with a temperature of 25 °C and relative humidity of approximately 80%. During this test, the electrolyte was kept at the same level by regularly adding up the electrolyte solution into the cells. The result is shown in Fig. 12. It was found that the power conversion efficiency showed a drastic decline at the first 4 weeks of aging that exhibit a decrease of efficiency from 4.6 to ca. 3.4%. However, the power conversion efficiency shows remarkable stability by retaining the efficiency at around 3.4% during aging up to 24 weeks. However, the efficiency is decreasing after that. We thought that a drastic decrease after 24 weeks of aging could be related to other factors, such as dye stability as the presence of color change, and device structure deformation during the filling of electrolytes during the aging process. If stable dye and a proper design of DSSC construction are obtained, long-time stability can be realized.

4. Conclusions

The co-metal element function in the Pt-based bimetallic nanostructures CEs in the charge transfer dynamics of the DSSCs has been investigated. It was found that the charge transfer resistance of the DSSCs was significantly reduced when the bimetallic CEs were used in the device. This is followed by the effective inhibition of photogenerated carrier recombination in the device, the result of enhanced carrier injection and transportation due to the increasing quantum chemical potential in the device. Such a process was driven by the existence of effective redox species diffusion over the CEs surface and the improvement of the electrocatalytic activity of the CEs. We found that the AuPt FNC CEs are the best-performed CEs that can deliver J_{sc}, V_{oc}, and FF values as high as 10.63 mAcm^{-2}, 1.00 V, and 0.43, respectively, were achieved. These give an equivalent PCE value of as high as 4.60%. This performance was 71% higher than the pristine Pt NC CEs. The present performance is still marginal when putting in the context of the recent reports, of which it could be related to the technical issues, including the device structure and construction, dye-loading, device area, and electrolyte stability issues. However, the present results provide a strategic understanding of how metal ion of different properties generates unique physicochemical properties in fibrous bimetallic CE, promoting enhancement in the charge transfer dynamic. High-performance DSSCs may be obtained using this CE when the related critical issues are solved.

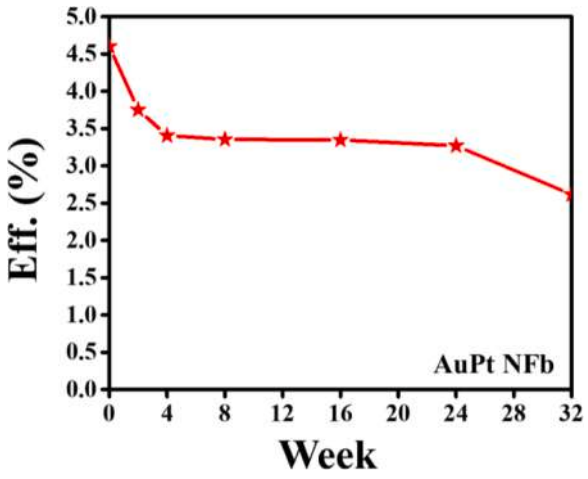

Fig. 12. The stability property of AuPt based device under aging in ambient condition, i.e. 25 °C and relative humidity of approximately 80%.

CRediT authorship contribution statement

Muhamad Adam Ramli: Resources, Investigation, Formal analysis, Data curation, Writing – original draft. **Elvy Rahmi Mawarnis:** Resources, Investigation, Formal analysis. **Marjoni Imamora Ali Umar:** Formal analysis, Investigation. **Mohd Yusri Abd Rahman:** Project administration, Validation, Supervision. **Vivi Fauzia:** Investigation, Formal analysis. **Muhammad Nurdin:** Formal analysis, Investigation. **Akrajas Ali Umar:** Conceptualization, Supervision, Methodology, Validation, Writing – review & editing, Funding acquisition.

Declaration of Competing Interest

There are no conflicts of interest to declare.

Acknowledgments

The authors would like to acknowledge the Ministry of Higher Education of Malaysia under research grant of FRGS/1/2019/STG02/UKM/02/3 and the Universiti Kebangsaan Malaysia for financial support under research grants GUP-2018–083. MAR is also grateful for the financial support received from Skim Zamalah Yayasan Canselor UKM 2018.

References

[1] N. Papageorgiou, Counter-electrode function in nanocrystalline photoelectrochemical cell configurations, Coord. Chem. Rev. 248 (2004) 1421–1446.

[2] V.J. Cybulskis, B.C. Bukowski, H.-.T. Tseng, J.R. Gallagher, Z. Wu, E. Wegener, A. J. Kropf, B. Ravel, F.H. Ribeiro, J. Greeley, Zinc promotion of platinum for catalytic light alkane dehydrogenation: insights into geometric and electronic effects, ACS Catal. 7 (2017) 4173–4181.

[3] A. Ali Umar, S.K. Md Saad, M. Mat Salleh, Scalable mesoporous platinum diselenide nanosheet synthesis in water, ACS Omega 2 (2017) 3325–3332.

[4] Q. Wang, H. Wang, Y. Yang, L. Jin, Y. Liu, Y. Wang, X. Yan, J. Xu, R. Gao, P. Lei, J. Zhu, Y. Wang, S. Song, H. Zhang, Plasmonic Pt superstructures with boosted near-infrared absorption and photothermal conversion efficiency in the second biowindow for cancer therapy, Adv. Mater. 31 (2019), 1904836.

[5] S. Yun, A. Hagfeldt, T. Ma, Pt-free counter electrode for dye-sensitized solar cells with high efficiency, Adv. Mater. 26 (2014) 6210–6237.

[6] M. Chen, L.-.L. Shao, X.-.W. Lv, G.-.C. Wang, W.-.Q. Yang, Z.-.Y. Yuan, X. Qian, Y.-.Y. Han, A.-.X. Ding, *In situ* growth of Ni-encapsulated and N-doped carbon nanotubes on N-doped ordered mesoporous carbon for high-efficiency triiodide reduction in dye-sensitized solar cells, Chem. Eng. J. 390 (2020), 124633.

[7] M. Chen, G.-.C. Wang, W.-.Q. Yang, Z.-.Y. Yuan, X. Qian, J.-.Q. Xu, Z.-.Y. Huang, A.-.X. Ding, Enhanced synergetic catalytic effect of Mo2C/NCNTs@ Co heterostructures in dye-sensitized solar cells: fine-tuned energy level alignment and efficient charge transfer behavior, ACS Appl. Mater. Interfaces 11 (2019) 42156–42171.

[8] M. Chen, G.-.C. Wang, L.-.L. Shao, Z.-.Y. Yuan, X. Qian, Q.-.S. Jing, Z.-.Y. Huang, D.-.L. Xu, S.-.X. Yang, Strategic design of vacancy-enriched Fe1−x S nanoparticles anchored on Fe3C-encapsulated and N-doped carbon nanotube hybrids for high-efficiency triiodide reduction in dye-sensitized solar cells, ACS Appl. Mater. Interfaces 10 (2018) 31208–31224.

[9] M. Chen, L.-.L. Shao, M.-.Y. Dong, X.-.W. Lv, Z.-.Y. Yuan, X. Qian, Y.-.Y. Han, A.-.X. Ding, Molecular-level synthesis of cobalt phosphide nanocrystals confined in highly nitrogen-doped mesoporous carbon electrocatalyst for highly efficient dye-sensitized solar cells, ACS Sustain. Chem. Eng. 8 (2020) 17245–17261.

[10] X. Qian, H. Liu, J. Yang, H. Wang, J. Huang, C. Xu, Co-Cu-WS x ball-in-ball nanospheres as high-performance Pt-free bifunctional catalysts in efficient dye-sensitized solar cells and alkaline hydrogen evolution, J. Mater. Chem. A 7 (2019) 6337–6347.

[11] H. Liu, X. Qian, Y. Niu, M. Chen, C. Xu, K.-.Y. Wong, Hierarchical Ni-MoSex@ $CoSe_2$ core-shell nanosphere as highly active bifunctional catalyst for efficient dye-sensitized solar cell and alkaline hydrogen evolution, Chem. Eng. J. 383 (2020), 123129.

[12] J. Yang, C. Zhang, Y. Niu, J. Huang, X. Qian, K.-.Y. Wong, N-doped C-CoS_2@ CoS_2/MoS_2 nano polyhedrons with hierarchical yolk-shelled structures as bifunctional catalysts for enhanced photovoltaics and hydrogen evolution, Chem. Eng. J. 409 (2021), 128293.

[13] F. Gong, X. Xu, Z. Li, G. Zhou, Z.-.S. Wang, $NiSe_2$ as an efficient electrocatalyst for a Pt-free counter electrode of dye-sensitized solar cells, Chem. Commun. 49 (2013) 1437–1439.

[14] A. Sarkar, A.K. Chakraborty, S. Bera, NiS/rGO nanohybrid: an excellent counter electrode for dye sensitized solar cell, Sol. Energy Mater. Sol. Cells 182 (2018) 314–320.

[15] O. Omelianovych, L.L. Larina, H.-.J. Oh, E. Park, V.-.D. Dao, H.-.S. Choi, Plasma-processed CoSn/RGO nanocomposite: a low-cost and sustainable counter electrode for dye-sensitized solar cells, Sol. Energy 201 (2020) 819–826.

[16] M. Rahman, A. Sulaiman, A. Umar, M. Salleh, Dye-sensitized solar cell (DSSC) utilizing reduced graphene oxide (RGO) films counter electrode: effect of graphene oxide (GO) content, J. Mater. Sci. Mater. Electron. 28 (2017) 1674–1678.

[17] H.H. Thi Vu, T.S. Atabaev, J.Y. Ahn, N.N. Dinh, H.-.K. Kim, Y.-.H. Hwang, Dye-sensitized solar cells composed of photoactive composite photoelectrodes with enhanced solar energy conversion efficiency, J. Mater. Chem. A 3 (2015) 11130–11136.

[18] Y.-.M. Lee, D.I. Kim, K.-.H. Hwang, S.H. Nam, J.-.H. Boo, Enhanced power conversion efficiency of dye-sensitized solar cells assisted with phosphor materials, Electron. Mater. Lett. 12 (2016) 512–516.

[19] A.Y.A. Al-She'irey, S.K.M. Saad, A.A. Umar, M.Y.A. Rahman, M.M. Salleh, (001) faceted-Ga-TiO_2 microtablet synthesis and its organic perovskite sensitized solar cells characterization, J. Alloys Compd. 674 (2016) 470–476.

[20] A.A. Shah, A.A. Umar, M.M. Salleh, Efficient quantum capacitance enhancement in DSSC by gold nanoparticles plasmonic effect, Electrochim. Act 195 (2016) 134–142.

[21] I. Iwantono, F. Anggelina, M. Saad, S. Khatijah, M.Y.A. Rahman, A.A. Umar, Influence of Ag ion adsorption on the photoactivity of ZnO nanorods for dye-sensitized solar cell application, Mater. Express 7 (2017) 312–318.

[22] S.K.M. Saad, A.A. Umar, M.Y.A. Rahman, M.M. Salleh, Porous Zn-doped TiO_2 nanowall photoanode: effect of Zn^{2+} concentration on the dye-sensitized solar cell performance, Appl. Surf. Sci. 353 (2015) 835–842.

[23] D. Dahlan, S.K.M. Saad, A.U. Berli, A. Bajili, A.A. Umar, Synthesis of two-dimensional nanowall of Cu-Doped TiO2 and its application as photoanode in DSSCs, Phys. E 91 (2017) 185–189.

[24] S. Ghasemi, S.R. Hosseini, M. Moalem-Banhangi, Preparation of electrochemically reduced graphene oxide/bimetallic copper-platinum nanohybrid as counter electrode for fabrication of dye-sensitized solar cell, J. Electroanal. Chem. 833 (2019) 242–250.

[25] J.-.S. Kim, V.-.D. Dao, L.L. Larina, H.-.S. Choi, Optimum alloying of bimetallic PtAu nanoparticles used as an efficient and robust counter electrode material of dye-sensitized solar cells, J. Alloys Compd. 682 (2016) 706–712.

[26] L. Wei, W. Chen, C. Jia, X. Yang, Y. Yang, Y. Dong, L. Liu, W. Song, Synthesis of CoNi bimetallic alloy nanoparticles wrapped in nitrogen-doped graphite-like carbon shells and their electrocatalytic activity when used in a counter electrode for dye-sensitized solar cells, J. Solid State Electrochem. 23 (2019) 1429–1442.

[27] F. Tao, S. Zhang, L. Nguyen, X. Zhang, Action of bimetallic nanocatalysts under reaction conditions and during catalysis: evolution of chemistry from high vacuum conditions to reaction conditions, Chem. Soc. Rev. 41 (2012) 7980–7993.

[28] D. Leishangthem, M.A.K. Yumkhaibam, P.S. Henam, S. Nagarajan, An insight into the effect of composition for enhance catalytic performance of biogenic Au/Ag bimetallic nanoparticles, J. Phys. Org. Chem. 31 (2018) e3815.

[29] J.K. Nørskov, T. Bligaard, J. Rossmeisl, C.H. Christensen, Towards the computational design of solid catalysts, Nat. Chem. 1 (2009) 37–46.

[30] E.R. Mawarnis, A.Ali Umar, M. Tomitori, A. Balouch, M. Nurdin, M.Z. Muzakkar, M. Oyama, Hierarchical bimetallic AgPt nanoferns as high-performance catalysts for selective acetone hydrogenation to isopropanol, ACS Omega 3 (2018) 11526–11536.

[31] A.A. Umar, E. Rahmi, A. Balouch, M.Y. Abd Rahman, M.M. Salleh, M. Oyama, Highly-reactive AgPt nanofern composed of {001}-faceted nanopyramidal spikes for enhanced heterogeneous photocatalysis application, J. Mater. Chem. A 2 (2014) 17655–17665.

[32] E. Rahmi, A.A. Umar, M.Y. Abd Rahman, M.M. Salleh, M. Oyama, Fibrous AuPt bimetallic nanocatalyst with enhanced catalytic performance, RSC Adv. 6 (2016) 27696–27705.

[33] S. Zhou, G.S. Jackson, B. Eichhorn, AuPt alloy nanoparticles for CO-tolerant hydrogen activation: architectural effects in Au-Pt bimetallic nanocatalysts, Adv. Funct. Mater. 17 (2007) 3099–3104.

[34] N. Sui, R. Yue, Y. Wang, Q. Bai, R. An, H. Xiao, L. Wang, M. Liu, W.Y. William, Boosting methanol oxidation reaction with Au@ AgPt yolk-shell nanoparticles, J. Alloys Compd. 790 (2019) 792–798.

[35] F.-.Q. Shao, J.-.J. Feng, Z.-.Z. Yang, S.-.S. Chen, J. Yuan, A.-.J. Wang, Cytosine assisted aqueous synthesis of AgPt hollow alloyed nanostructures as highly active electrocatalyst for ethylene glycol oxidation and hydrogen evolution, Int. J. Hydrog. Energy 42 (2017) 24767–24775.

[36] X. Zhou, Y. Gan, J. Du, D. Tian, R. Zhang, C. Yang, Z. Dai, A review of hollow Pt-based nanocatalysts applied in proton exchange membrane fuel cells, J. Power Sources 232 (2013) 310–322.

[37] Q. Shao, P. Wang, T. Zhu, X. Huang, Low dimensional platinum-based bimetallic nanostructures for advanced catalysis, Acc. Chem. Res. 52 (2019) 3384–3396.

[38] S.-.C. Lim, M.-.C. Hsiao, M.-.D. Lu, Y.-.L. Tung, H.-.Y. Tuan, Synthesis of germanium–platinum nanoparticles as high-performance catalysts for spray-deposited large-area dye-sensitized solar cells (DSSC) and the hydrogen evolution reaction (HER), Nanoscale 10 (2018) 16657–16666.

[39] Y. Xiao, G. Han, Efficient hydrothermal-processed platinum–nickel bimetallic nano-catalysts for use in dye-sensitized solar cells, J. Power Sources 294 (2015) 8–15.

[40] Y. Xiao, G. Han, Y. Li, M. Li, J.-.Y. Lin, Three-dimensional hollow platinum–nickel bimetallic nanoframes for use in dye-sensitized solar cells, J. Power Sources 278 (2015) 149–155.

[41] Y. Xiao, G. Han, R. Wu, Y. Li, M. Li, Efficiently cubic platinum-cobalt bimetallic nano-catalysts for use in low-cost dye-sensitized solar cells, Electrochim. Act 174 (2015) 770–777.

[42] K.-.H. Bae, E. Park, V.-.D. Dao, H.-.S. Choi, PtZn nanoalloy counter electrodes as a new avenue for highly efficient dye-sensitized solar cells, J. Alloys Compd. 702 (2017) 449–457.

[43] K. Yun, H.-.S. Nam, S. Kim, Categorization of atomic mixing patterns in bimetallic nanoparticles by the energy competition, Phys. Chem. Chem. Phys. 22 (2020) 7787–7793.

[44] J.-.H. Zhong, X. Jin, L. Meng, X. Wang, H.-.S. Su, Z.-.L. Yang, C.T. Williams, B. Ren, Probing the electronic and catalytic properties of a bimetallic surface with 3 nm resolution, Nat. Nanotechnol. 12 (2017) 132.

[45] A.A. Umar, M. Oyama, Synthesis of palladium nanobricks with atomic-step defects, Cryst. Growth Des. 8 (2008) 1808–1811.

[46] A. Ali Umar, M. Oyama, M. Mat Salleh, B. Yeop Majlis, Formation of highly thin, electron-transparent gold nanoplates from nanoseeds in ternary mixtures of cetyltrimethylammonium bromide, poly (vinyl pyrrolidone), and poly (ethylene glycol), Cryst. Growth Des. 10 (2010) 3694–3698.

[47] A. Balouch, A.A. Umar, S.T. Tan, S. Nafisah, S.K. Md Saad, M.M. Salleh, M. Oyama, Fibrous, ultra-small nanorod-constructed platinum nanocubes directly grown on the ITO substrate and their heterogeneous catalysis application, RSC Adv. 3 (2013) 19789–19792.

[48] M.A. Ramli, S.K.M. Saad, E.R. Mawarnis, M.I.A. Umar, P.S. Menon, M.Y. Abd Rahman, A.A. Umar, Facile charge transfer in fibrous PdPt bimetallic nanocube counter electrodes, New J. Chem. 43 (2019) 11148–11156.

[49] D. Dahlan, M.A. Ramli, K. Fiqrian, S.K.M. Saad, M. Oyama, A.A. Umar, Thermal impact on (001) faceted anatase TiO_2 microtablets and nanowalls's lattices and its effect on the photon to current conversion efficiency, J. Phys. Chem. Solids 127 (2019) 213–223.

[50] S.K. Md Saad, A. Ali Umar, M.I. Ali Umar, M. Tomitori, M.Y. Abd. Rahman, M. Mat Salleh, M. Oyama, Two-dimensional, Hierarchical Ag-doped TiO_2 nanocatalysts: effect of the metal oxidation state on the photocatalytic properties, ACS Omega 3 (2018) 2579–2587.

[51] S.K.M. Saad, A.A. Umar, H.Q. Nguyen, C.F. Dee, M.M. Salleh, M. Oyama, Porous (001)-faceted Zn-doped anatase TiO_2 nanowalls and their heterogeneous photocatalytic characterization, RSC Adv. 4 (2014) 57054–57063.

[52] S.K.M. Saad, A.A. Umar, H.Q. Nguyen, C.F. Dee, M.M. Salleh, M. Oyama, Porous (001)-faceted Zn-doped anatase TiO_2 nanowalls and their heterogeneous photocatalytic characterization, RSC Adv. 4 (2014) 57054–57063.

[53] S.K.M. Saad, A.A. Umar, M.Y.A. Rahman, M.M. Salleh, Porous Zn-doped TiO_2 nanowall photoanode: effect of Zn^{2+} concentration on the dye-sensitized solar cell performance, Appl. Surf. Sci. 353 (2015) 835–842.
[54] M.Y.A. Rahman, A.A. Umar, S.K.M. Saad, M.M. Salleh, Effect of NH_3 concentration on the performance of nitrogen doped TiO_2 photoelectrochemical cell, Int. J. Electrochem. Sci. 7 (2012) 7855–7865.
[55] A.Y.A. Al-She'irey, S.K.M. Saad, A.A. Umar, M.Y.A. Rahman, M.M. Salleh, (001) faceted-Ga-TiO_2 microtablet synthesis and its organic perovskite sensitized solar cells characterization, J. Alloys Compd. 674 (2016) 470–476.
[56] A. Ali Umar, S. Nafisah, S.K. Md Saad, S. Tee Tan, A. Balouch, M. Mat Salleh, M. Oyama, Poriferous microtablet of anatase TiO_2 growth on an ITO surface for high-efficiency dye-sensitized solar cells, Sol. Energy Mater. Sol. Cells 122 (2014) 174–182.
[57] I. Iwantono, S.K.M. Saad, F. Anggelina, A. Awitdrus, M.A. Ramli, A.A. Umar, Enhanced charge transfer activity in Au nanoparticles decorated ZnO nanorods photoanode, Phys. E 111 (2019) 44–50.
[58] A.A. Shah, A.A. Umar, M.M. Salleh, Efficient quantum capacitance enhancement in DSSC by gold nanoparticles plasmonic effect, Electrochim. Act 195 (2016) 134–142.
[59] A.A. Shah, A.A. Umar, M.M. Salleh, Porous (001)-faceted anatase TiO_2 nanorice thin film for efficient dye-sensitized solar cell, EPJ Photovolt. 7 (2016) 70501.
[60] E. Mawarnis, A. Umar, Fibrous bimetallic silver palladium and ruthenium palladium nanocrystals exhibit an exceptionally high active catalytic process in acetone hydrogenation, Mater. Today Chem. 14 (2019), 100178.
[61] X. Yang, Q. Yang, J. Xu, C.-.S. Lee, Bimetallic PtPd nanoparticles on nafion–graphene film as catalyst for ethanol electro-oxidation, J. Mater. Chem. 22 (2012) 8057–8062.
[62] X. Niu, C. Chen, H. Zhao, Y. Chai, M. Lan, Novel snowflake-like Pt–Pd bimetallic clusters on screen-printed gold nanofilm electrode for H_2O_2 and glucose sensing, Biosens. Bioelectron. 36 (2012) 262–266.
[63] M.A. Rahim, R.A. Hameed, M. Khalil, The role of a bimetallic catalyst in enhancing the electro-catalytic activity towards methanol oxidation, J. Power Sources 135 (2004) 42–51.
[64] B. Qiu, L. Cai, Y. Wang, Z. Lin, Y. Zuo, M. Wang, Y. Chai, Fabrication of nickel–cobalt bimetal phosphide nanocages for enhanced oxygen evolution catalysis, Adv. Funct. Mater. 28 (2018), 1706008.
[65] X. Wang, L. Altmann, J.r. Stöver, V. Zielasek, M. Bäumer, K. Al-Shamery, H. Borchert, J.r. Parisi, J. Kolny-Olesiak, Pt/Sn intermetallic, core/shell and alloy nanoparticles: colloidal synthesis and structural control, Chem. Mater. 25 (2013) 1400–1407.
[66] K. Hirakawa, T. Kaneko, N. Toshima, Kinetics of spontaneous bimetallization between silver and noble metal nanoparticles, Chem. Asian J. 13 (2018) 1892–1896.
[67] X. Peng, Q. Pan, G.L. Rempel, S. Wu, Synthesis, characterization, and application of PdPt and PdRh bimetallic nanoparticles encapsulated within amine-terminated poly (amidoamine) dendrimers, Catal. Commun. 11 (2009) 62–66.
[68] S. Tokonami, N. Morita, K. Takasaki, N. Toshima, Novel synthesis, structure, and oxidation catalysis of Ag/Au bimetallic nanoparticles, J. Phys. Chem. C 114 (2010) 10336–10341.
[69] A.A. Umar, X. Zhang, S.K.M. Saad, N.A. Abd Malek, K. Liu, N. Alias, N.A. Abdullah, X. Li, F. Liu, Z. Shi, Enhancing the interfacial carrier dynamic in perovskite solar cells with an ultra-thin single-crystalline nanograss-like TiO_2 electron transport layer, J. Mater. Chem. A 8 (2020) 13820–13831.
[70] Z. Wang, X. Liu, H. Jiang, X. Zhou, L. Zhang, F. Pan, X. Qiao, D. Ma, W. Ma, L. Ding, Organic solar cells based on high hole mobility conjugated polymer and nonfullerene acceptor with comparable bandgaps and suitable energy level offsets showing significant suppression of Jsc–Voc Trade-Off, Sol. RRL 3 (2019), 1900079.
[71] P. Chao, L. Liu, J. Qu, Q. He, S. Gan, H. Meng, W. Chen, F. He, Overcoming the trade-off between Voc and Jsc: asymmetric chloro-substituted two-dimensional benzo [1, 2-b: 4, 5-b′] dithiophene-based polymer solar cells, Dyes Pigments 162 (2019) 746–754.
[72] N.A.A. Malek, N. Alias, A.A. Umar, X. Zhang, X. Li, S.K.M. Saad, N.A. Abdullah, H. Zhang, Z. Weng, Z. Shi, Enhanced charge transfer in atom-thick 2H–WS_2 nanosheets' electron transport layers of perovskite solar cells, Sol. RRL 4 (2020), 2000260.
[73] N.K. Elumalai, A. Uddin, Open circuit voltage of organic solar cells: an in-depth review, Energy Environ. Sci. 9 (2016) 391–410.
[74] X. Huang, Z. Wang, R. Knibbe, B. Luo, S.A. Ahad, D. Sun, L. Wang, Cyclic voltammetry in lithium–sulfur batteries—challenges and opportunities, Energy Technol. 7 (2019), 1801001.
[75] L. Kavan, J.-.H. Yum, M. Graetzel, Graphene-based cathodes for liquid-junction dye sensitized solar cells: electrocatalytic and mass transport effects, Electrochim. Act 128 (2014) 349–359.
[76] T. Sruthi, T. Kartick, Route to achieving enhanced quantum capacitance in functionalized graphene based supercapacitor electrodes, J. Phys. Condens. Matter 31 (2019), 475502.
[77] Q. Yang, P. Yang, J. Duan, X. Wang, L. Wang, Z. Wang, Q. Tang, Ternary platinum alloy counter electrodes for high-efficiency dye-sensitized solar cells, Electrochim. Act 190 (2016) 85–91.
[78] A. Monga, R.A. Rather, B. Pal, Enhanced co-catalytic effect of Cu-Ag bimetallic core-shell nanocomposites imparted to TiO_2 under visible light illumination, Sol. Energy Mater. Sol. Cells 172 (2017) 285–292.
[79] C. Costentin, J.-.M. Savéant, Towards an intelligent design of molecular electrocatalysts, Nat. Rev. Chem. 1 (2017) 1–8.
[80] J.-.X. Wu, W.-.W. Yuan, M. Xu, Z.-.Y. Gu, Ultrathin 2D nickel zeolitic imidazolate framework nanosheets for electrocatalytic reduction of CO_2, Chem. Commun. 55 (2019) 11634–11637.
[81] L. Kavan, Z. Vlckova Zivcova, M. Zlamalova, S.M. Zakeeruddin, M. Grätzel, Electron-selective layers for dye-sensitized solar cells based on TiO_2 and SnO_2, J. Phys. Chem. C 124 (2020) 6512–6521.
[82] V.V. Pavlishchuk, A.W. Addison, Conversion constants for redox potentials measured versus different reference electrodes in acetonitrile solutions at 25 °C, Inorg. Chim. Act 298 (2000) 97–102.
[83] F.W. Vance, R.V. Slone, C.L. Stern, J.T. Hupp, Comparative absorption, electroabsorption and electrochemical studies of intervalence electron transfer and electronic coupling in cyanide-bridged bimetallic systems: ancillary ligand effects, Chem. Phys. 253 (2000) 313–322.
[84] G.I. Tóth, G. Tegze, T. Pusztai, L. Gránásy, Heterogeneous crystal nucleation: the effect of lattice mismatch, Phys. Rev. Lett. 108 (2012), 025502.
[85] L. Kavan, P. Liska, S.M. Zakeeruddin, M. Grätzel, Low-temperature fabrication of highly-efficient, optically-transparent (FTO-free) graphene cathode for Co-mediated dye-sensitized solar cells with acetonitrile-free electrolyte solution, Electrochim. Act 195 (2016) 34–42.
[86] T. Daeneke, T.-.H. Kwon, A.B. Holmes, N.W. Duffy, U. Bach, L. Spiccia, High-efficiency dye-sensitized solar cells with ferrocene-based electrolytes, Nat. Chem. 3 (2011) 211–215.